PCCP

PAPER

Cite this: *Phys. Chem. Chem. Phys.*, 2024, **26**, 11933

The effect of water in THF/water mixtures on CMC, aggregation sizes, and fluorescence quenching of a new calix[4]resorcinarene macrocycle†

María Virginia Sosa,[a] Kashif Hussain,[b] Eduardo D. Prieto,[ad] Tatiana Da Ros,[c] M. Raza Shah[b] and Ezequiel Wolcan*[a]

Received 16th February 2024,
Accepted 13th March 2024

DOI: 10.1039/d4cp00687a

rsc.li/pccp

This study explores how water content modulates the self-assembly and fluorescence behavior of a novel calixarene, **C1**. **C1** forms large, flattened structures in pure THF, but water addition triggers a transition to smaller, unimodal clusters. A critical micellar concentration (CMC) is identified, decreasing with increasing water content. Fluorescence quenching is observed upon water addition, attributed to nonradiative deactivation. These findings highlight water as a key regulator of **C1**'s assembly and fluorescence, paving the way for further development of water-responsive calixarene systems.

1. Introduction

Surfactants are versatile molecules with hydrophobic and hydrophilic portions, widely used in various industries.[1–7] They act as excipients in pharmaceutical and cosmetic formulations, stabilize dispersed systems, increase drug solubility, and can be used as drug permeability enhancers.[8–12] Their self-assembling properties lead to the formation of micelles, and the critical micelle concentration (CMC) is a crucial parameter for these molecules.[13] When the concentration of the surfactants falls below the CMC, they form a coating on interfacial surfaces, reducing surface tension across gas, liquid, and solid interfaces. However, when the concentration exceeds the CMC, the surfactants organize themselves into distinct spherical and cylindrical micellar mesostructures, which disperse throughout the bulk aqueous environment as a colloidal solution.[9] Resorcinarenes and calixarenes are macrocyclic blocks that are easily available and can act as supramolecular hosts. They are made up of aromatic rings derived from resorcinol or phenol, which are connected by carbon bridges. They can be used in their natural or functionalized forms to create receptors, cavitands, and capsules for various purposes, such as sensing, storage, reaction nanovessels, and biological applications.[14] In particular, resorcin[4]arenes consist of four resorcinol rings bridged by four –C(R)– H units. When the R substituent at the carbon bridge is a long aliphatic chain, they are inherently amphiphilic.

The all-*cis* isomer of *C*-methyl resorcin[4]arene is the most thermally stable. It has a soft π-donor cavity made up of phenolic rings and hydroxyl groups on the upper rim of the molecule. These groups can act as hydrogen bond donors. Although the crown conformation is the most stable due to the four intramolecular hydrogen bonds between the phenolic hydroxyl groups, scoop, and boat conformation have also been found in solids (Scheme 1).[15,16]

Due to the relative flexibility of resorcinarenes, two or more conformations can convert in equilibrium.[17,18] Resorcinarenes and calixarenes exhibit an interesting structural feature where their conformation and mobility can change, affecting their ability to form host–guest complexes. Restricting their conformational mobility can improve the selectivity and affinity of the host. Moreover, the self-assembly properties of amphiphilic resorcinarenes, such as water solubility and aggregate sizes, can also be affected by conformation mobility. By redirecting hydrophobic groups towards water, self-assembly can reduce the conformational mobility of resorcinarenes and calixarenes.[19–23] Controlled changes to the conformation of resorcinarenes can create motors and switches.[24]

Resorcinarenes exhibit fascinating self-assembly behavior influenced by their functionalization. MacGillivray and Atwood identified a recurring hexameric structure in *C*-methylcalix[4]resorcinarene,

---

[a] *Instituto de Investigaciones Fisicoquímicas Teóricas y Aplicadas (INIFTA, UNLP, CCT La Plata-CONICET), Diag. 113 y 64, Sucursal 4, C.C. 16, (B1906ZAA) La Plata, Argentina. E-mail: ewolcan@inifta.unlp.edu.ar*
[b] *H.E.J. Research Institute of Chemistry, International Center for Chemical and Biological Sciences, University of Karachi, 75270, Karachi, Pakistan*
[c] *INSTM, Department of Chemical and Pharmaceutical Sciences, University of Trieste, Via L. Giorgieri 1, 34127, Trieste, Italy*
[d] *Departamento de Cs. Biológicas, Facultad de Ciencias Exactas (UNLP), Instituto Ciencias de la Salud, Universidad Nacional Arturo Jauretche (UNAJ), Argentina*

† Electronic supplementary information (ESI) available. See DOI: **https://doi.org/10.1039/d4cp00687a**

stabilized by hydrogen bonds, which persists even in apolar solvents.[25] Larger resorcinarenes with specific substituents can also form similar hexamers, while octamers with a cubic arrangement have been observed in toluene.[26–28] Studies reveal a range of aggregate sizes (N_{agg}) for tetramethylene sulfonate-substituted calix[4]resorcinarenes, demonstrating the influence of functionalization on self-assembly.[29] Functionalization plays a key role, with hydrogen bonding and metal coordination being the most common drivers. Vesicles, micelles, and nanoparticles are observed in water, while AFM studies revealed unexpected layered structures in amphiphilic calixarenes.[30] This highlights the tunable nature of resorcinarene self-assembly, allowing researchers to design materials with tailored properties for various applications.

Another important consequence of molecular aggregation in calixarenes and resorcinarenes is related to its effect on their fluorescence. When compared to diluted solutions, luminophores may exhibit reduced, unchanged, or enhanced emissions in the aggregated state. The reduced or enhanced emissions resulting from aggregation are called aggregated-caused quenching (ACQ) and aggregated-induced emission (AIE), respectively. ACQ is more common than AIE, and from the viewpoint of real-world application, researchers usually look forward to avoiding ACQ while pursuing AIE.[31] There are, however, many situations in which ACQ can be beneficial, for instance in bioimaging of drug nanocarriers[32] in biocompatible pH sensors[33] and ion sensors.[34] In particular, ACQ in calixarenes and resorcinarenes have been used in the sensing of Cu(II) and Co(II) ions[35,36] and an organic pollutant like 4-nitrotoluene.[37]

This study explores the influence of water content on the self-assembly and photophysical properties of a novel calix[4]-resorcinarene macrocycle, **C1**. **C1** readily dissolves in THF, but water addition above 20% triggers aggregation, evidenced by increased light scattering. Absorption spectroscopy suggests a critical micellar concentration (CMC) exceeding 0.1 mM for water contents between 20% and 33%, decreasing with further water increase. AFM and DLS reveal flattened, layered aggregates in pure THF, which transform into smaller, more uniform clusters with increasing water content. Fluorescence quenching is observed upon water addition, suggesting aggregation-induced quenching (ACQ). Theoretical calculations provide insights into the electronic transitions responsible for **C1**'s photophysical properties. These findings establish water as a key modulator of **C1**'s self-assembly and fluorescence behavior, paving the way for further exploration of water-responsive calixarene systems.

2. Results and discussion

2.1. Synthesis of compound C1

The compound **C1** was synthesized through a reaction between compound **(a)** and resorcinol (see Scheme 2). See ESI† for characterization by ESI-MS, NMR, FTIR, and physical characterization.

2.2. Absorption spectroscopy in THF and THF/H_2O mixtures and aggregation

The calix[4]resorcinarene macrocycle compound, **C1**, experiences some minor absorbance changes within 1 h–24 h after dissolution in THF or THF/H_2O mixtures. Absorption changes in a similar time-lapse of related resorcin[4]arenes due to aggregation phenomena have been previously reported.[38] Therefore, all the experimental work reported hereafter was performed after the stabilization of the absorbance spectra, *i.e.* 24 h subsequently **C1** solutions were prepared. The calix[4]-resorcinarene macrocycle **C1**, when dissolved in THF displays an intense absorption band in the UV region (λ_{max} = 285 nm, ε_{285nm} = 2.5 × 10^4 M^{-1} cm^{-1}) with a slightly less intense shoulder at 291 nm in the 1–5 × 10^{-5} M range of concentrations (Fig. 1). At concentrations higher than 10^{-4} M a broad unstructured and much less intense tail is developed between 330 and 600 nm. The absorption bands of **C1** compare well with the spectral features of a resorcin[4]arene with R = CH_3–$(CH_2)_{14}$ in the same visible region of the spectrum.[39]

It is expected that resorcin[4]arene, which lacks chromophoric groups, such as **C1** and other similar resorcin[4]arenes, and only contains dialkoxy- and dialkyl-substituted benzene rings should be colorless.[39,40] However, it has been observed that when the concentration of this compound is increased above 10^{-4} M, a much less intense tail develops between 350 and 600 nm. This phenomenon may be caused by slow aggregation (*vide infra*). A similar absorption spectroscopy study was conducted

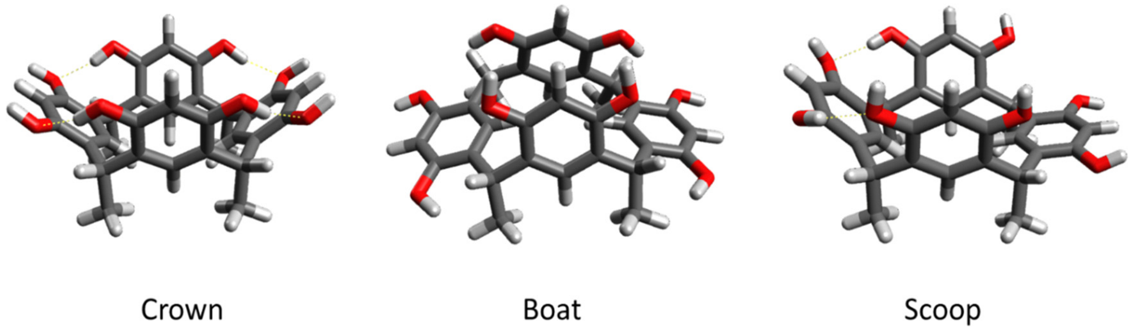

Scheme 1 Crown, boat, and scoop conformations of all *cis* *C*-methyl resorcin[4]arene.

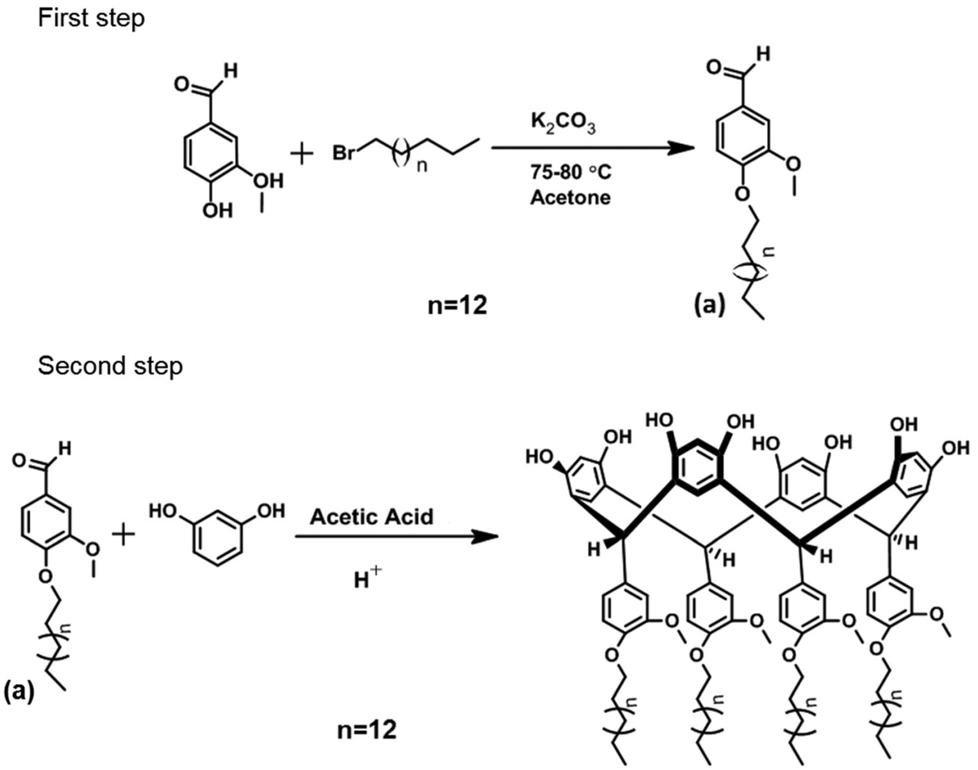

Scheme 2 The schematic illustration shows the synthesis of a functionalized calix[4]resorcinarene macrocycle through a two-step reaction.

with **C1** solutions in the 1×10^{-5} – 2×10^{-4} M range of concentrations in THF/H_2O mixtures of different H_2O content (between 20–95%). The absorption spectra of **C1** solutions in varying concentrations of water mixed with THF were analyzed. The spectra were observed at 0, 20, 33, 47, 53, 60, 67, 88, and 95% concentrations of H_2O. The results are shown in Fig. 1 and Fig. S5 (ESI†). It was noticed that as the water content increased from 0 to 20%, the tail between 330 and 600 nm in neat THF solutions increased relative to the maximum at $\lambda_{\max}$ = 285 nm, as seen in Fig. 1. Absorbance *vs.* concentration plots at 285, 355, and 600 nm at 0, 20, 33, 47, 53, 60, 67, 88, and 95% concentrations of H_2O are shown in Fig. 2 and Fig. S6 (ESI†). When the concentration of **C1** was increased in THF solutions or THF with 20% water, an increase in absorbance at 355 nm was observed.

Moreover, the slope of the line for $A_{285\text{nm}}$ *vs.* **C1** concentration was almost identical for both pure THF solutions and THF solutions containing 20% water. The absorbance between 600 and 700 nm did not show any significant increase even when the water content in the THF solution was at 20% and **C1** was increased. However, when the water content was 33%, there was an increase in absorption in the range of 600–700 nm, which indicates light scattering. Additionally, a down curvature in the plot of $A_{285\text{nm}}$ *vs.* **C1** concentration was observed above 0.1 mM concentrations, indicating deviation from linearity. Light scattering became visible above 53% water content, as seen in the flat portion of spectra between 350 and 700 nm, which increased proportionally with **C1** concentration. Furthermore, the slopes of the lines for $A_{285\text{nm}}$ *vs.* **C1** concentration at 47%, 53%, and 95% of water were roughly half the slope value for neat THF. The light scattering process was the most intense at 60% water content, with absorbances at 285 nm higher than in neat THF. In addition, the highest slopes of the $A_{600\text{nm}}$ *vs.* **C1** concentration lines were observed at a water content of 60%.

All the absorption spectra of Fig. 1 and Fig. S5 (ESI†) were analyzed by chemometric techniques to retrieve, from the absorbance matrix, the concentration profiles and the spectra of each contributing factors. These methods can be applied to bilinear spectroscopic data from a chemical reaction to provide information about composition changes in an evolving system. In the present work, we used the multivariate curve resolution coupled to alternating least-squares (MCR-ALS) algorithm to simultaneously estimate concentration and spectral profiles. MCR-ALS extracts useful information from the experimental data matrix $A(i \times j)$ by the iterative application of the following matrix product: $A = CS^T + E$ where $C(i \times n)$ is the matrix of the concentrations profiles, $S^T(n \times j)$ is that containing the spectral profiles, and $E(i \times j)$ represents the error matrix. The indexes i, n, and j denote the samples, absorbing factors, and recorded wavelengths, respectively.[41] To perform the MCR-ALS analysis, we took into account the non-negative absorption spectra and non-negative concentration constraints. It was necessary to consider three independent factors (n = 3) to accurately replicate all of the experimental data. These three factors, which are F1, F2, and F3, have spectral profiles of E(F1), E(F2), and E(F3), along with relative concentrations of C(F1), C(F2), and C(F3). The spectral profiles and the dependence of relative

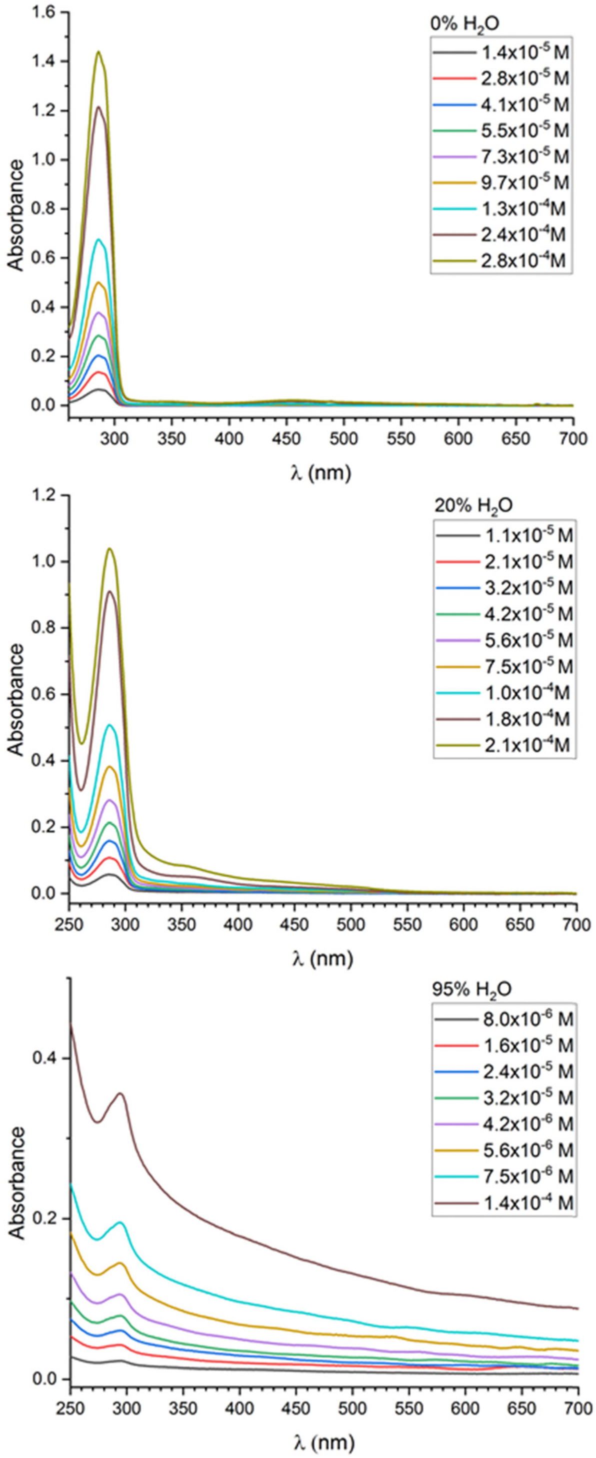

Fig. 1 Absorption spectra of **C1** at several concentrations in THF/H$_2$O solutions at 0, 20 and 95% of H$_2$O.

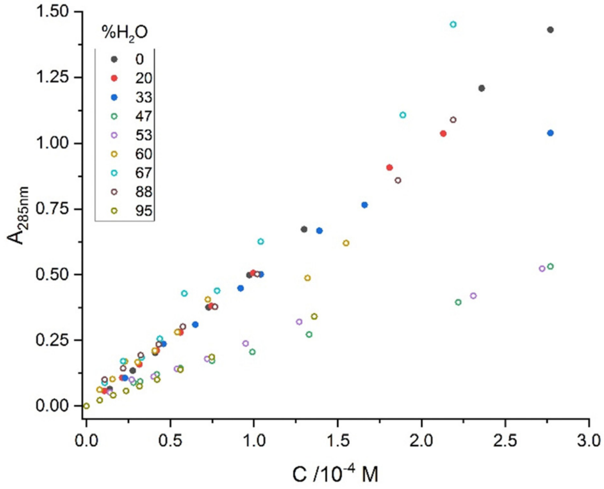

5 nm.

Fig. 2 Absorbance *vs.* concentration of **C1** at 285 nm.

concentrations on the total concentration of **C1** and water content of the solution are shown in Fig. S7–S16 (ESI†).

The spectral features of F1 are identical to those of **C1** in pure THF. The spectral features of F2 account for the absorption tail that appears between 330 and 600 nm in pure THF solutions, in comparison to the peak at $\lambda_{\max}$ = 285 nm, as a result of increased water content from 0 to 20%. The flat spectral shape of F3 corresponds to the scattered light component in the absorption spectra.

It is observed that only C(F1) in pure THF is required to explain the absorption spectra dependence on **C1** concentration, and a linear relationship exists between C(F1) and **C1** concentration. At a water content of 20%, the primary contribution to the absorption spectra is from F1, but F2 also makes significant additional contributions. The linear relationship between C(F1) and **C1** concentration begins to curve downwards at approximately 2 × 10^{-4} M. At a water content of 33%, the primary contribution to the absorption spectra is from F1, with minor contributions from F2 and F3. The increase in the concentration of F3 at **C1** concentrations between 1.5–3 × 10^{-4} M indicates the appearance of light scattering effects. The linear relationship between C(F1) and **C1** concentration begins to curve downwards at approximately 1 × 10^{-4} M. At a water content of 47%, the primary contributions to the absorption spectra are from F1 and F3, with negligible participation of F2. The concentration of C(F3) becomes higher than that of C(F3) at **C1** concentrations above 5 × 10^{-5} M, and the scattering of light becomes prevalent. As the concentration of **C1** increases, the value of C(F3) also increases steadily. At a water content of 53%, F3 dominates absorption spectra with minor contributions from F1 and F2. C(F3) increases as **C1** concentration increases. Between water content of 60–95%, F2 and F3 absorption spectra dominate, with F1 contribution being negligible. As **C1** concentration increases, C(F3) and C(F2) also increase steadily. It appears that there is a critical micellar concentration (CMC) at concentrations above 0.1 mM, as indicated by the downward curvature in the plot of C(F1) *versus* **C1** concentration. This CMC is observed for water contents between 20% and 33%. Additionally, the CMC seems to decrease as the percentage of water increases.

An extended multiplicative signal correction (EMSC) preprocessing method allowed a separation of physical light-scattering effects from chemical light absorbance effects in spectra form from powders or turbid solutions.[42,43] After pretreating the UV-vis absorption data of Fig. 1 and Fig. S5 (ESI†) with EMSC, the scattering effects on the absorbance of the solutions were removed, resulting in the presentation of chemical effects only. Fig. 3 presents the results. Fig. 3a displays the EMSC pretreated data of Fig. 1 and Fig. S5 (ESI†). It can be observed that the spectra maxima shift from 284 to 291 nm. This trend was also noticed in Fig. 1 and Fig. S5 (ESI†), but light scattering effects in the absorption spectra obscured the tendency. Data in Fig. 3a were decomposed by chemometric techniques into two factors (F4 and F5) based on their spectral profiles (Fig. 3b) and relative concentrations (C(F4) and C(F5); Fig. 3c). F4 has an absorption maximum of 285 nm and F5 peaks at 289 nm. C(F4) and C(F5) represent the average concentrations of F4 and F5 at each **C1** concentration in Fig. 1 and Fig. S5 (ESI†) after EMSC pretreatment and chemometric analysis. Fig. 3c presents the dependence of C(F4) and C(F5) on the percentage of H_2O. C(F4) and C(F5) show two different patterns. In the first pattern, the concentration of F5 increases from 0% and reaches a plateau at around 20–30% of water. After that, the concentration of F5 increases sigmoidally until it reaches the maximum value at 95% of water. The pattern of F4 concentration mirrors that of F5: it decreases from 0% to a plateau around 20–30% water and then continues to decrease until reaching the minimum value. Both C(F4) and C(F5) *vs.* % of water concentration profiles cross at ∼ 47%. When the water content in a THF solution of **C1** exceeds 47%, the molecule starts to aggregate regardless of its concentration, as suggested by the crossing of C(F4) and C(F5) profiles. This is consistent with the observation that the critical micellar concentration (CMC) decreases as the water content increases. This suggests that the increased water content plays a dominant role in driving aggregation, making the concentration of **C1** less relevant above a certain water threshold.

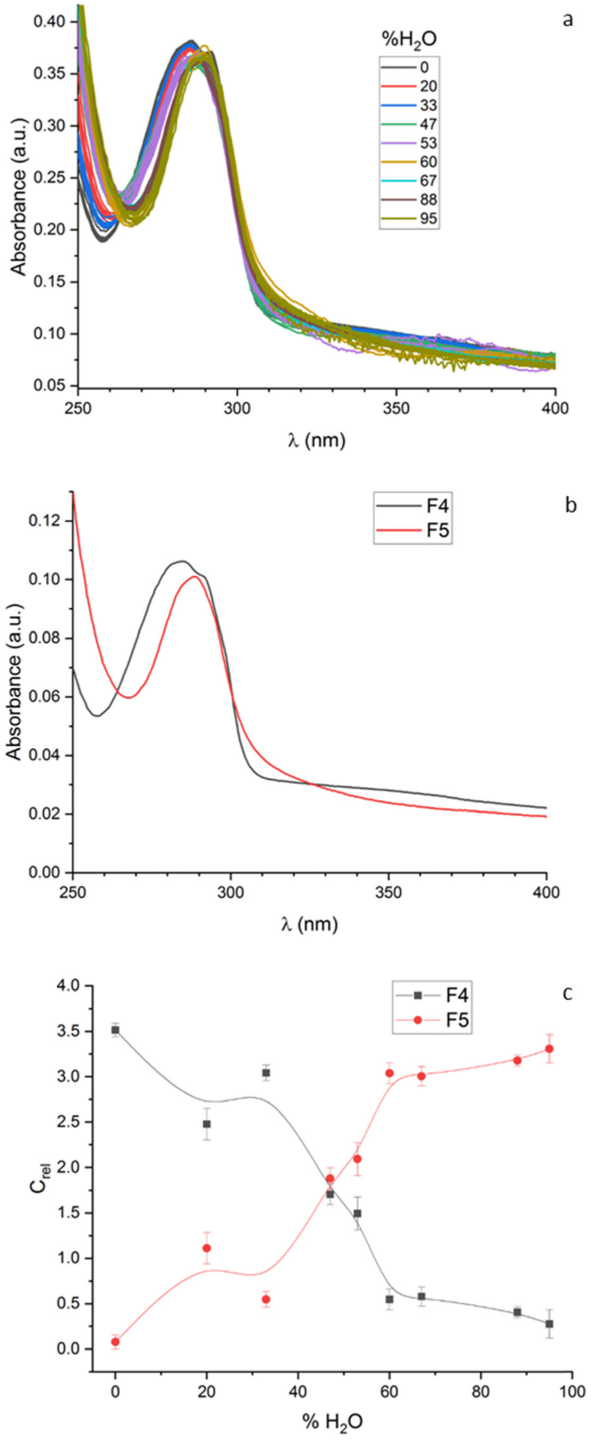

Fig. 3 (a) EMSC pretreated UV data. (b) F4 and F5 decomposed data. (c) F4 and F5 relative concentration *vs.* % H_2O.

Dynamic light scattering confirmed the presence of aggregates, with significant size variability and large particles detected in pure THF. However, the poor data quality precluded reporting numerical values for the hydrodynamic diameter (d_h) sizes. In contrast, DLS analysis at 53% water concentration showed a bimodal size distribution with two populations: large aggregates (1001 ± 145 nm diameter, contributing 94.4% to the total scattering) and smaller factors (2.88 ± 0.04 nm diameter, contributing 5.3%). Unfortunately, determining the polydispersity index for this sample was not possible. At 95% water concentration, DLS indicated an unimodal size distribution with a d_h of 166 ± 2 nm and a polydispersity index of 0.10 ± 0.01. See Fig S17 and S18 and Tables S1 and S2 (ESI†) for detailed data. In DLS experiments, the dependence of aggregation size on water concentration can be compared to the insights gained from absorption spectroscopy. When the water concentration is below 50–60%, DLS reveals a bimodal size distribution. This indicates the presence of two types of aggregates. Large aggregates dominate the distribution with an average hydrodynamic diameter (d_h) of 1001 ± 145 nm. Small aggregates contribute much less to the overall scattering and have an average d_h of 2.88 ± 0.04 nm. This observation aligns with the first pattern identified in the EMSC/chemometric analysis of the absorption profiles shown in Fig. 3. These figures suggest the presence of two distinct factors at lower water concentrations. On the other hand, when the water concentration reaches 95%, DLS shows an unimodal size distribution with a d_h of 166 ± 2 nm. This finding is consistent with the observation from absorption spectroscopy that F5, the factors associated with larger aggregates, reaches its maximum concentration at around 95% water content. These results highlight the complementary nature of DLS and absorption spectroscopy for studying aggregation behavior. While DLS provides direct information about particle size distribution, absorption spectroscopy offers insights into the composition and relative concentration of different factors present in the solution. By combining these techniques, we gain a comprehensive understanding of how aggregation changes with water content.

2.3. Fluorescence

When a solution of **C1** in neat THF is optically excited at its high energy absorption maximum (λ_{ex} = 285 nm), fluorescence is observed with a peak emission wavelength of approximately 319 nm (Fig. 4a). Upon the addition of water, the fluorescence intensity begins to decrease, indicating quenching. At 95% water content, the luminescence intensity is reduced by a factor of 10 compared to pure THF. Luminescence quantum yields were measured using the integrating sphere method and are listed in Table 1 as a function of water percentage. Fig. 4b displays two key plots: the ratio of initial fluorescence to measured fluorescence (Φ_0/Φ) *versus* water content and the fractional quenching ($1 - \Phi/\Phi_0$) *versus* water content. The upward deviation from a linear Stern–Volmer plot observed in the Φ_0/Φ *versus* water content plot even at low water percentages signifies the presence of a static quenching process. Comparing the Stern–Volmer (Φ_0/Φ) and fractional quenching ($1 - \Phi/\Phi_0$) *versus* water content reveals a critical water concentration of approximately 50%, where the slope of the Φ_0/Φ plot changes. This suggests a significant alteration in the dominant factors at this water content. The plot of fractional quenching exhibits two inflection points, one around 47% and another around 80% water content, further highlighting the complex dependence of quenching on water concentration. Fig. S19 (ESI†) shows normalized fluorescence spectra at various water percentages. As water is added, the emission maximum shifts from 319 nm to 308 nm, and the spectral shape broadens. This suggests changes in the underlying molecular environment and potentially the presence of different emitting factors. Chemometric analysis of the fluorescence spectra in Fig. S19 (ESI†) reveals the presence of three distinct factors contributing to the overall emission: F6, F7, and F8 (Fig. S20, ESI†). Their concentration profiles are shown in Fig. S21 (ESI†). Both F6 and F7 contribute to the fluorescence observed in pure THF, with F7 exhibiting a higher initial contribution. As the water content increases, the contribution of F7 becomes increasingly dominant, reaching a maximum of 60% water. Beyond this point, the contribution of F7 decreases significantly, becoming negligible at water concentrations above 67%. In contrast, the contribution of F6 increases steadily between 60% and 92% water, displaying a bell-shaped dependence with a peak of around 80%. The presence of F8 only becomes significant at water concentrations above 80%, and at 95% water content, it is the only factor contributing to the overall fluorescence. These observations demonstrate the complex interplay between water content, aggregation behavior, and the relative contribution of different emitting factors in **C1** solutions.

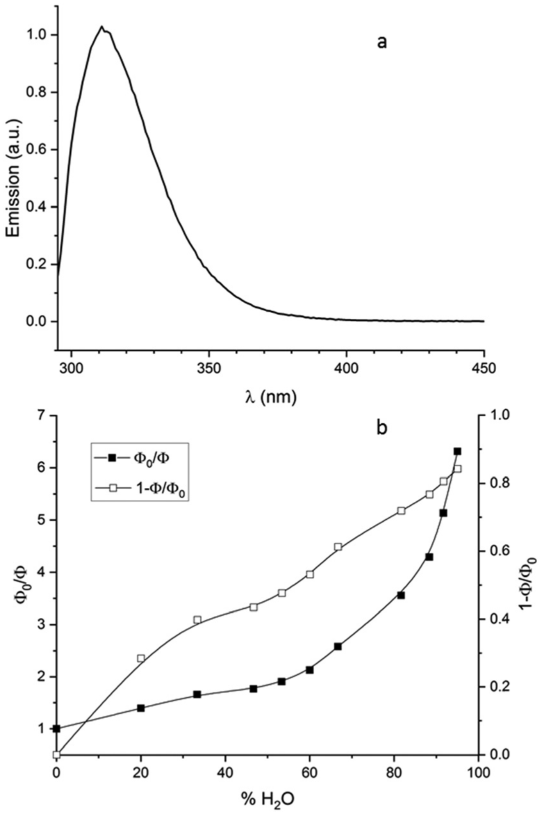

Fig. 4 (a) Luminescence spectra of **C1** in pure THF and (b) ■ Φ_0/Φ and □ $1 - \Phi/\Phi_0$ values as a function of % H_2O.

The fluorescence decay of **C1** required two exponential functions to be fitted properly. The longer lifetime (τ_{long}) was mostly consistent, regardless of the water content, at around 1.1–1.3 nanoseconds for water content between 0 to 95%. The shorter lifetime (τ_{short}), however, varied between 0.5 and 0.2 nanoseconds and decreased as the water content increased, as shown in Table 1. At 0% H_2O, the longer lifetime contributed 60% of the total relative amplitude, while the shorter lifetime contributed 40%. As the water content increased, the relative amplitude remained roughly at the same levels up to 80% water. Between 80% and 95% water content, the relative amplitude of the longer lifetime started to decrease, and that of the shorter lifetime increased. Eventually, at a water content of 95%, the relative amplitude of the longer lifetime was 20%, while that of the shorter lifetime was 80%. Amplitude average lifetimes,[44] $\tau_{ave\text{-}amp}$, were computed with τ_{long} and τ_{short}. The value of amplitude average lifetimes decreased from 0.4–0.5 ns for water contents between 0–20% to 0.2 ns at 95% of water content. Using $\tau_{ave\text{-}amp}$, the average radiative (k_r) and radiationless (k_{nr}) deactivation rate constants were calculated by applying the following formulas:

$$k_r = \phi_f/\tau_{ave\text{-}amp}$$

$$k_{nr} = (1 - \phi_f)/\tau_{ave\text{-}amp}$$

Table 1 Fluorescence quantum yields (Φ), luminescence lifetimes (τ_{short} and τ_{long}), amplitude average lifetimes ($\tau_{ave-amp}$), radiative (k_r), and radiationless (k_{nr}) deactivation rate constants of **C1** in THF at different % H_2O

% H_2O	Φ	τ_{short}/ns	τ_{long}/ns	$\tau_{ave-amp}$/ns	$k_r/10^8\ s^{-1}$	$k_{nr}/10^9\ s^{-1}$
0	0.15 ± 0.02	0.40 ± 0.06	1.1 ± 0.1	0.65 ± 0.04	2.3 ± 0.2	1.30 ± 0.09
20	0.11 ± 0.01	0.47 ± 0.06	1.2 ± 0.1	0.67 ± 0.03	1.63 ± 0.09	1.34 ± 0.08
33	0.091 ± 0.009	0.45 ± 0.02	1.13 ± 0.04	0.66 ± 0.01	1.38 ± 0.04	1.38 ± 0.04
47	0.086 ± 0.009	0.49 ± 0.03	1.33 ± 0.01	0.753 ± 0.005	1.14 ± 0.02	1.21 ± 0.02
53	0.079 ± 0.008	0.40 ± 0.10	1.2 ± 0.2	0.65 ± 0.09	1.2 ± 0.2	1.4 ± 0.2
60	0.071 ± 0.007	0.32 ± 0.05	1.17 ± 0.08	0.50 ± 0.06	1.4 ± 0.2	1.8 ± 0.2
67	0.059 ± 0.006	0.33 ± 0.08	1.2 ± 0.2	0.48 ± 0.08	1.2 ± 0.2	2.0 ± 0.4
82	0.043 ± 0.004	0.32 ± 0.08	1.0 ± 0.1	0.48 ± 0.08	0.9 ± 0.2	2.0 ± 0.4
88	0.035 ± 0.004	0.20 ± 0.08	1.2 ± 0.2	0.25 ± 0.07	1.4 ± 0.4	4 ± 1
92	0.030 ± 0.003	0.22 ± 0.04	1.1 ± 0.1	0.26 ± 0.04	1.2 ± 0.2	3.8 ± 0.7
95	0.024 ± 0.002	0.17 ± 0.03	1.05 ± 0.04	0.21 ± 0.04	1.2 ± 0.3	5 ± 1

In neat THF, the values of k_r and k_{nr} are 2.3×10^8 and $1.3 \times 10^9\ s^{-1}$, respectively. However, upon adding water, the value of k_r decreases to $0.9–1.6 \times 10^8\ s^{-1}$ while the value of k_{nr} increases to a range between 1.8×10^9 and $5 \times 10^9\ s^{-1}$ as shown in Table 1.

2.4. AFM analysis of C1 aggregates

AFM analysis of an amphiphilic calixarene revealed two distinct particle populations. The first comprised surprising round objects roughly 200 nm in diameter. However, the most unexpected finding was the presence of a second type of structure: a layered system with a height of 1.5–2 nm, resembling supported lipid bilayers.[45] The morphology of **C1** aggregates was investigated using AFM. Samples were prepared by placing **C1** solutions on mica surfaces and drying them under vacuum. In neat tetrahydrofuran (THF), AFM revealed the presence of flattened round bilayer sheets with a trimodal distribution. The largest clusters exhibited a diameter (d) of 605 ± 317 nm and a height (h) of 47 ± 34 nm. Intermediate-sized clusters displayed d = 399 ± 99 nm and h = 15 ± 9 nm, while the smallest clusters had d = 336 ± 107 nm and h = 8 ± 5 nm (Fig. 5a and Fig. S22, ESI†). Notably, all clusters exhibited pronounced flattening, resembling supported lipid bilayers reported by Shahgaldian *et al.*[45] Adding water significantly impacted the aggregate morphology. At 53% water content (Fig. 5b and Fig. S23, ESI†), the number and size of larger clusters decreased significantly. A predominantly unimodal distribution with d = 302 ± 89 nm and h = 9 ± 5 nm remained, indicating that water addition flattened and shrunk the larger clusters. Further increasing the water content to 95% led to a near-complete disappearance of large clusters (Fig. 5c and Fig. S24, ESI†). Instead, a prevalent unimodal distribution with even smaller dimensions (d = 72 ± 19 nm, h = 2.8 ± 0.5 nm) emerged. Interestingly, the morphological properties of **C1** observed in Fig. 5 and Fig. S22–S24 (ESI†) resemble the self-assembly behavior of *para*-carboxy modified amphiphilic calixarene in water.[45]

2.5. Comparison of AFM and DLS results

The sizes of **C1** aggregates measured by AFM differed significantly from those obtained by dynamic light scattering (DLS). DLS consistently revealed aggregate sizes much larger than those observed by AFM. See Table 2 for a summary of aggregate dimensions measured by DLS and AFM. This suggests that different aggregate structures exist in the solution and the solid state. According to the computational section, DFT calculations have determined that the average volume of each **C1** molecule is ~2.5 nm^3. Based on the data in Table 2, it can be roughly estimated that the number of **C1** molecules per aggregate ranges from approximately 10^6 to 10^8 for solution aggregates and from approximately 10^3 to 10^5 for solid-state aggregates. The exact number depends on the water content and dimensions of the different aggregates. This is a rough estimation as only two conformers, *i.e.* **C1-c** and **C1-b**, were considered to calculate the average volume of each **C1** molecule. Importantly, the smallest cluster height observed at 95% water (2.8 ± 0.5 nm) is similar to the calculated total length of the **C1** molecule (approximately 2.8 nm). This suggests that the smallest clusters consist of single **C1** molecules arranged in a flattened configuration.

2.6. Aggregation caused quenching in THF/H_2O mixtures

Experiments employing absorption spectroscopy, dynamic light scattering, atomic force microscopy, and both steady-state and time-resolved fluorescence revealed the phenomenon of aggregation caused by quenching (ACQ) in **C1** molecules due to increasing water content in THF solutions. Fluorescence and absorbance spectroscopy revealed the presence of three distinct factors whose concentrations depend on both **C1** concentration and the percentage of water, further suggesting the coexistence of different clusters of varying sizes. These varying sizes were confirmed by dynamic light scattering and atomic force microscopy analysis. The plot of $1 - (\Phi/\Phi_0)$ *versus* % H_2O (Fig. 4b) exhibits two distinct regions, each with an inflection point. The first inflection point occurs at around 40–50% water, while the second appears at approximately 80–85%. This suggests that the quenching mechanism is altered by the formation of large clusters when water concentration exceeds 33%, followed by a decrease in size with a subsequent increase in water content. The deviation from a linear Stern–Volmer plot, even at low percentages of water, indicates a static quenching process. The quenching of **C1** fluorescence by water appears to proceed in a two-step process. Initially, **C1** fluorescence is quenched by water up to 40%, where a plateau of $1 - (\Phi/\Phi_0)$ is reached at

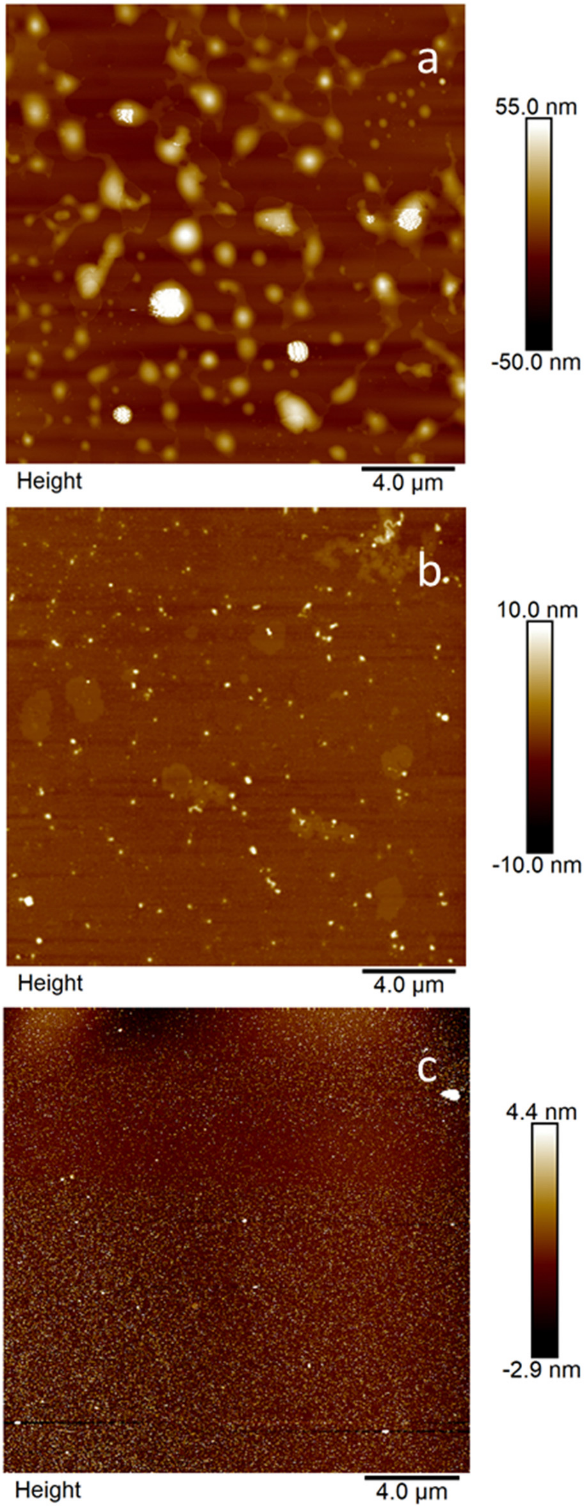

Fig. 5 AFM images of **C1** in: (a) pure THF, (b) THF (47%)/H_2O (53%) and (c) THF (5%)/H_2O (95%).

50% water. Beyond this point, the slope of $1 - (\Phi/\Phi_0)$ increases again as the percentage of water is further increased. The static quenching observed in the fluorescence of **C1** upon the addition of water is likely associated with an enhancement of nonradiative deactivation due to π–π stacking of neighboring resorcinol molecules. This stacking is exacerbated by H-bond formation and chromophore crowding as the water content is increased. Within **C1** clusters, there may be room for a specific number of **C1** chromophores whose fluorescence cannot be quenched by further addition of water. This phenomenon is further supported by the seven factors Fi (i = 1–7) whose spectral shapes and concentration profiles were recovered from absorption and fluorescence spectroscopy with EMSC/MCR-ALS techniques. These factors essentially describe the same phenomenon: the solvent-induced surfactant aggregation of **C1** molecules in different cluster shapes, which ultimately leads to ACQ. The complete set of absorption data requires 3 factors to explain, which tentatively represents the absorption features of multiple chemical species both inside and outside the clusters, as well as the absorption features corresponding to the scattering effects. However, after the EMSC, the number of factors reduces to 2, as the scattering effects are eliminated by this method, leaving only the chemical effects. In the chemometric analysis of the fluorescence data, 3 factors are required to reproduce the spectral features of the fluorescence spectra at different water contents of the solutions, in line with the absorption spectroscopy data. Interestingly, the shape of the $1 - (\Phi/\Phi_0)$ *versus* % H_2O plot closely resembles that of C_{rel} of F5 in Fig. 3c. This suggests that the factors retrieved from EMSC/MCR-ALS analysis of absorption spectra are directly responsible for the photophysical behavior of **C1** fluorescence upon the addition of water to THF solutions. The study also revealed a competitive fluorescence relaxation of **C1** molecules relative to those free in solution, with **C1** molecules forming clusters of flattened round shape or micellar geometries. The aggregation state, which is dependent on the solvent, appears to exhibit flattened round layer sheets at water concentrations between 20% and 60%, and spherical micelles at water concentrations above 90%, as depicted in Scheme 3. The k_{r} values are largely independent of the water content of the solutions. However, the k_{nr} values increase steadily at water contents above 60%, indicating the presence of some dynamic components in the quenching process in addition to the static one mentioned above (Table 1).

2.7. Molecular electronic structure

The molecular structures of **C1** and **Cr** were optimized using DFTBA methods. **Cr** is a reduced version of calix[4]resorcinarene where the long hydrocarbon chains of **C1** were replaced by a methyl moiety. The optimization was done at both the crown (c) and the boat (b) conformations of the macrocycle. The optimized structures obtained were **C1-b**, **C1-c**, **Cr-b**, and **Cr-c**. Additionally, four dimers constructed from **Cr-b** and **Cr-c**, *i.e.*, **D1-b**, **D2-b**, **D1-c**, and **D2-c** (refer to Fig. S25, ESI†) were also optimized using DFTBA methods. The molecule has a cavity on its upper rim consisting of phenolic rings and hydroxyl groups. The cavity is approximately ellipsoidal with minor and major axis dimensions of about 1.1 nm and 1.7 nm, respectively. The entire length of the molecule from the end of the R chain to the bottom of the **C1** crown structure (**C1-c**) is approximately 2.8 nm. Based on calculated volumes, the estimated volume of each molecule is either 2.3 or 2.7 nm^3 for

Table 2 Hydrodynamic radii (DLS) and diameters and heights of the flattened round layer sheets (AFM) from solutions of **C1** prepared from THF or THF/H_2O mixtures

(%) Water	DLS d_h (nm)	AFM diameter (nm)	AFM height (nm)
0	—	Trimodal distribution 605 ± 317 nm 399 ± 99 nm 336 ± 107 nm	Trimodal distribution 47 ± 34 nm 15 ± 9 nm 8 ± 5 nm
53	Bimodal distribution 1001 ± 145 nm (94.4%) 2.88 ± 0.04 nm (5.3%) P.I. = n.d.	302 ± 89 nm	9 ± 5 nm
95	Unimodal distribution 166 ± 2 nm P.I. = 0.10 ± 0.01	72 ± 19 nm	2.8 ± 0.5 nm

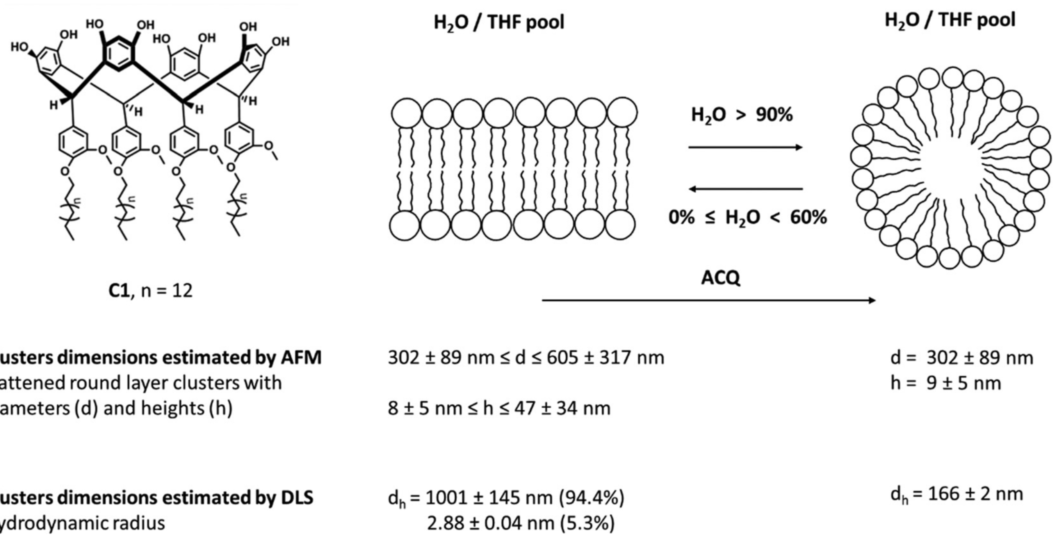

Scheme 3 Flattened round layer sheets and micelles, with their respective dimensions of aggregates, formed by **C1** in THF/H_2O mixtures, induce aggregation caused quenching (ACQ).

C1-c or **C1-b**, respectively. Assuming a "mean" volume of ~2.5 nm^3 for the **C1** molecule, the number of molecules present in each aggregate (as mentioned earlier) can be estimated.

TD-DFT calculations were carried out at the B3LYP/6-31-G(d,p)/PCM (THF) level of theory for all of the optimized structures mentioned above. The calculated absorption spectra can be compared with the experimental ones in THF (Fig. 6). Some general observations can be made: (i) the electronic structures of **C1-b** and **C1-c** poorly describe the experimental absorption spectra, with a blue shift of approximately 20 nm and 30 nm, respectively, of the calculated absorption maxima relative to the experimental one; (ii) substitution of long methyl chains by $-CH_3$ does not affect the performance in predicting the absorption spectrum, *i.e.*, the calculated spectra of **C1-b** (**C1-c**) and **Cr-b** (**Cr-c**) are nearly the same; (iii) in the crown conformations, new absorptions (as shoulders in the calculated spectra) appear at longer wavelengths; and (iv) the best description of the experimental absorption spectra is given by the crown dimers, with differences between calculated and experimental maxima around 10–14 nm. In all dimers, crowns, and boats, intermolecular H-bonds occur. Regarding the electronic structure, the crown and boat conformations differ mainly due to the formation of intramolecular hydrogen bonds between resorcinols in the former. When two **Cr** molecules are close to each other and a dimer is formed, intermolecular hydrogen bonds are created. The presence of intermolecular hydrogen bonds is more significant than intramolecular hydrogen bonds when predicting the accurate absorption spectrum of **C1** with the help of TD-DFT calculations.

We will now delve into the electronic transitions of **C1-b**, **C1-c**, **Cr-b**, **Cr-c**, **D1-b**, **D1-c**, **D2-b**, and **D2-c**. Please refer to Tables S3–S10 (ESI†) for the calculated electronic transitions. For each electronic structure, we have selected the two or three most intense singlet–singlet excitations that have contributed the most to the calculated spectra of Fig. 6. The natural transition orbital (NTO) analysis has given us a more concise orbital representation of molecular orbitals (MOs) for those selected transitions. Tables S11–S18 (ESI†) show the H − 3, H − 2, H − 1, H, L, L + 1, L + 2, and L + 3 MOs from NTO analysis for the selected electronic transitions of **C1-b**, **C1-c**,

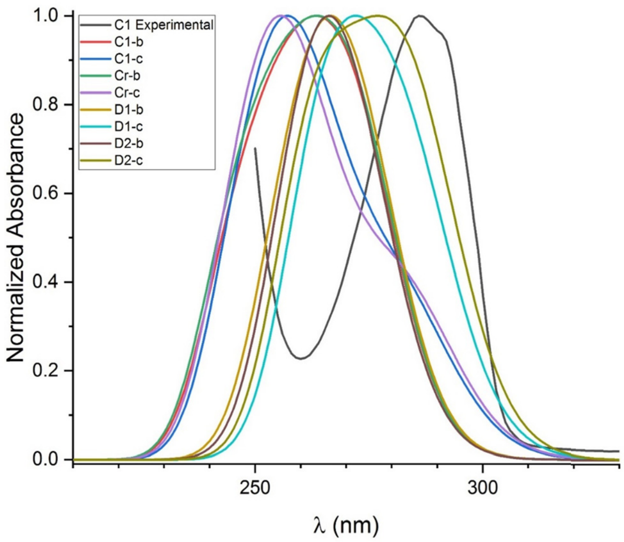

Fig. 6 The experimental absorption spectrum of **C1** in THF and the calculated absorption for all the optimized structures. The structures were optimized using DFTBA methods. TD-DFT calculations were performed at the B3LYP/6-31-G(d,p)/PCM (THF) level of theory on the optimized structures. Please refer to the text for further details.

Cr-b, **Cr-c**, **D1-b**, **D1-c**, **D2-b**, and **D2-c**. As the electronic structure of **D2-c** has better represented the experimental absorption spectra of **C1**, we will discuss the NTO analysis of it.

The electronic transitions Nr. 8 (λ_{calc} = 282.54 nm), Nr. 9 (λ_{calc} = 281.29 nm) and Nr.10 (λ_{calc} = 281.24 nm) are the three ones that best represent the overall calculated spectra for **D2-c** with calculated oscillator strengths of f_{osc} = 0.05 for all them (See Table S10, ESI†). In the three electronic transitions, NTO analysis of those electronic transitions (Table S18, ESI†) shows that the electron density is transferred mainly from the four resorcinols at the crown cavity to the $(CH_3\text{–}O)_2\text{–}(C_6H_5)\text{–}$ moiety in one of the two bridged molecules, *i.e.* an intramolecular charge transfer in one of the bridged molecules. Since boat and crown conformations can be in equilibrium in THF solutions, the observed absorption spectra of **C1** can be the result of many conformations, some of them similar to **D2-c** and others that may be more complex, with aggregates with N_{agg} higher than 2.

3. Conclusions

This investigation reveals a significant influence of water content on the self-assembly behavior of a novel calixarene, **C1**. We demonstrate a water-mediated transformation, where **C1** transitions from forming large aggregates in pure THF to well-defined, smaller clusters as water concentration increases. This precise control over **C1**'s self-assembly is accompanied by a phenomenon known as aggregation-induced quenching (ACQ), which effectively modulates **C1**'s fluorescence intensity. While ACQ may initially appear to be a limitation, it presents a unique opportunity for sensor design. Prior research has established the utility of ACQ in calixarenes and resorcinarenes for selective detection of specific targets, including Cu(II) and Co(II) ions and organic pollutants like 4-nitrotoluene. Our findings suggest that **C1**, with its water-tunable ACQ, possesses significant potential as a platform for the development of next-generation sensors with precise fluorescence control.

Conflicts of interest

There are no conflicts to declare.

Acknowledgements

This work was supported in part by CONICET (PIP 112-2013-01-00236CO), ANPCyT (PICT 2018-03341) and UNLP (11/X779 and 11/X679) Argentina. E. W. is a Research Member of CONICET (Argentina). M. V. S thanks ANPCyT and CONICET for a research scholarship. EC is acknowledged for the INFUSION project grant N. 734834 under H2020-MSCA-RISE-2016.

References

1 E. Weiand, F. Rodriguez-Ropero, Y. Roiter, P. H. Koenig, S. Angioletti-Uberti, D. Dini and J. P. Ewen, Effects of surfactant adsorption on the wettability and friction of biomimetic surfaces, *Phys. Chem. Chem. Phys.*, 2023, **25**, 21916–21934.
2 Z. Sumer and A. Striolo, Manipulating molecular order in nematic liquid crystal capillary bridges: Via surfactant adsorption: Guiding principles from dissipative particle dynamics simulations, *Phys. Chem. Chem. Phys.*, 2018, **20**, 30514–30524.
3 H. Lee and T. J. Jeonb, The binding and insertion of imidazolium-based ionic surfactants into lipid bilayers: The effects of the surfactant size and salt concentration, *Phys. Chem. Chem. Phys.*, 2015, **17**, 5725–5733.
4 A. M. S. Jorge, G. M. C. Silva, J. A. P. Coutinho and J. F. B. Pereira, Unravelling the molecular interactions behind the formation of PEG/PPG aqueous two-phase systems, *Phys. Chem. Chem. Phys.*, 2024, **26**, 7308–7317.
5 Y. Han and Y. Wang, Aggregation behavior of gemini surfactants and their interaction with macromolecules in aqueous solution, *Phys. Chem. Chem. Phys.*, 2011, **13**, 1939–1956.
6 A. Bhadani, M. Tani, T. Endo, K. Sakai, M. Abe and H. Sakai, New ester based gemini surfactants: the effect of different cationic headgroups on micellization properties and viscosity of aqueous micellar solution, *Phys. Chem. Chem. Phys.*, 2015, **17**, 19474–19483.
7 J. Penfold and R. K. Thomas, *Phys. Chem. Chem. Phys.*, 2022, **24**, 8553–8577.
8 M. Dasgupta and N. Kishore, Establishing Structure Property Relationship in Drug Partitioning into and Release from Niosomes: Physical Chemistry Insights with Anti-Inflammatory Drugs, *J. Phys. Chem. B*, 2017, **121**, 8902–8918.
9 D. J. Speer, M. Salvador-Castell, Y. Huang, G. Y. Liu, S. K. Sinha and A. N. Parikh, Surfactant-Mediated Structural

Modulations to Planar, Amphiphilic Multilamellar Stacks, *J. Phys. Chem. B*, 2023, **127**, 7497–7508.

10 A. M. Percebom, G. A. Ferreira, D. R. Catini, J. S. Bernardes and W. Loh, Phase Behavior Controlled by the Addition of Long-Chain n-Alcohols in Systems of Cationic Surfactant/Anionic Polyion Complex Salts and Water, *J. Phys. Chem. B*, 2018, **122**, 4861–4869.

11 C. M. C. Faustino, A. R. T. Calado and L. Garcia-Rio, New urea-based surfactants derived from α,ω-amino acids, *J. Phys. Chem. B*, 2009, **113**, 977–982.

12 S. Ristori, S. Rossi, G. Ricciardi and G. Martini, Fluorinated/hydrogenated mixed vesicles as carrier of model biomolecules: A spectroscopic study, *J. Phys. Chem. B*, 1997, **101**, 8507–8512.

13 D. Romano Perinelli, M. Cespi, N. Lorusso, G. Filippo Palmieri, G. Bonacucina and P. Blasi, Surfactant Self-Assembling and Critical Micelle Concentration: One Approach Fits All?, *Langmuir*, 2020, **36**, 5745–5753.

14 K. Stefańska, H. Jędrzejewska, M. Wierzbicki, A. Szumna and W. Iwanek, The Inverse Demand Oxa-Diels-Alder Reaction of Resorcinarenes: An Experimental and Theoretical Analysis of Regioselectivity and Diastereoselectivity, *J. Org. Chem.*, 2016, **81**, 6018–6025.

15 H. Mansikkamäki, M. Nissinen and K. Rissanen, C-Methyl resorcin[4]arene packing motifs with alkyl ammonium salts: From molecular capsules to channels and tubes, *CrystEngComm*, 2005, **7**, 519–526.

16 B. Q. Ma and P. Coppens, A novel scoop-shaped conformation of C-methylcalix[4]resorcinarene in a bilayer structure, *Chem. Commun.*, 2002, 424–425.

17 A. G. S. Hogberg, Two stereoisomeric macrocyclic resorcinol-acetaldehyde condensation products, *J. Org. Chem.*, 2002, **45**, 4498–4500.

18 L. Abis, E. Dalcanale, A. Du Vosel and S. Spera, Nuclear magnetic resonance elucidation of ring-inversion processes in macrocyclic octaols, *J. Chem. Soc., Perkin Trans. 2*, 1990, 2075–2080.

19 K. Helttunen, P. Prus, M. Luostarinen and M. Nissinen, Interaction of aminomethylated resorcinarenes with rhodamine B, *New J. Chem.*, 2009, **33**, 1148–1154.

20 K. Helttunen, K. Salorinne, T. Barboza, H. C. Barbosa, A. Suhonen and M. Nissinen, Cation binding resorcinarene bis-crowns: the effect of lower rim alkyl chain length on crystal packing and solid lipid nanoparticles, *New J. Chem.*, 2012, **36**, 789–795.

21 K. Helttunen, E. Nauha, A. Kurronen, P. Shahgaldian and M. Nissinen, Conformational polymorphism and amphiphilic properties of resorcinarene octapodands, *Org. Biomol. Chem.*, 2011, **9**, 906–914.

22 K. Helttunen and P. Shahgaldian, Self-assembly of amphiphilic calixarenes and resorcinarenes in water, *New J. Chem.*, 2010, **34**, 2704–2714.

23 K. Helttunen, N. Moridi, P. Shahgaldian and M. Nissinen, Resorcinarene bis-crown silver complexes and their application as antibacterial Langmuir–Blodgett films, *Org. Biomol. Chem.*, 2012, **10**, 2019.

24 B. H. Huisman, F. C. J. M. Van Veggel and D. N. Reinhoudt, Supramolecular chemistry at interfaces, *Pure Appl. Chem.*, 1998, **70**, 1985–1992.

25 L. R. MacGillivray and J. L. Atwood, A chiral spherical molecular assembly held together by 60 hydrogen bonds, *Nature*, 1997, **389**, 469–472.

26 Q. Zhang, L. Catti and K. Tiefenbacher, Catalysis inside the Hexameric Resorcinarene Capsule, *Acc. Chem. Res.*, 2018, **51**, 2107–2114.

27 S. Fujii, R. Miyake, L. De Campo, J. H. Lee, R. Takahashi and K. Sakurai, Structural Polymorphism of Resorcinarene Assemblies, *Langmuir*, 2020, **36**, 6222–6227.

28 S. Fujii and K. Sakurai, Structural Analysis of an Octameric Resorcinarene Self-Assembly in Toluene and its Morphological Transition by Temperature, *J. Phys. Chem. Lett.*, 2021, **12**, 6464–6468.

29 V. V. Syakaev, Y. V. Shalaeva, E. K. Kazakova, Y. E. Morozova, N. A. Makarova and A. I. Konovalov, Aggregation and complexation in a series of tetramethylenesulfonate-substituted calix[4]resorcinarenes, *Colloid J.*, 2012, **74**(3), 346–355.

30 J. L. Liu, M. Sun, Y. H. Shi, X. M. Zhou, P. Z. Zhang, A. Q. Jia and Q. F. Zhang, Functional modification, self-assembly and application of calix[4]resorcinarenes, *J. Inclusion Phenom. Macrocyclic Chem.*, 2022, **1**, 1–33.

31 J. Mei, N. L. C. Leung, R. T. K. Kwok, J. W. Y. Lam and B. Z. Tang, Aggregation-Induced Emission: Together We Shine, United We Soar!, *Chem. Rev.*, 2015, **115**, 11718–11940.

32 J. Qi, X. Hu, X. Dong, Y. Lu, H. Lu, W. Zhao and W. Wu, Towards more accurate bioimaging of drug nanocarriers: turning aggregation-caused quenching into a useful tool, *Adv. Drug Delivery Rev.*, 2019, **143**, 206–225.

33 B. Fu, J. Huang, D. Bai, Y. Xie, Y. Wang, S. Wang and X. Zhou, Label-free detection of pH based on the i-motif using an aggregation-caused quenching strategy, *Chem. Commun.*, 2015, **51**, 16960–16963.

34 B. A. Makwana, D. J. Vyas, K. D. Bhatt, S. Darji and V. K. Jain, Novel fluorescent silver nanoparticles: sensitive and selective turn off sensor for cadmium ions, *Appl. Nanosci.*, 2016, **6**, 555–566.

35 K. D. Bhatt, D. J. Vyas, B. A. Makwana, S. M. Darjee and V. K. Jain, Highly stable water dispersible calix[4]pyrrole octa-hydrazide protected gold nanoparticles as colorimetric and fluorometric chemosensors for selective signaling of Co(II) ions, *Spectrochim. Acta, Part A*, 2014, **121**, 94–100.

36 B. A. Makwana, D. J. Vyas, K. D. Bhatt and V. K. Jain, Selective sensing of copper (II) and leucine using fluorescent turn on – off mechanism from calix[4]resorcinarene modified gold nanoparticles, *Sens. Actuators, B*, 2017, **240**, 278–287.

37 U. Panchal, K. Modi, S. Dey, U. Prajapati, C. Patel and V. K. Jain, A resorcinarene-based ''turn-off'' fluorescence sensor for 4-nitrotoluene: Insights from fluorescence and 1H NMR titration with computational approach, *J. Lumin.*, 2017, **184**, 74–82.

38 I. V. Lijanova, I. Moggio, E. Arias, R. Vazquez-Garcia and M. Martínez-García, Highly fluorescent dendrimers containing

stilbene, and 4-styryistilbene with resorcinarene cores: Synthesis and optical properties, *J. Nanosci. Nanotechnol.*, 2007, **7**, 3607–3614.

39 A. Saha, S. K. Nayak, S. Chattopadhyay and A. K. Mukherjee, Study of Charge Transfer Interactions of a Resorcin[4]arene with [60]- and [70]Fullerenes by the Absorption Spectrometric Method, *J. Phys. Chem. A*, 2004, **108**, 8223–8228.

40 M. He, R. J. Johnson, J. O. Escobedo, P. A. Beck, B. J. Melancon, W. D. Treleaven, R. M. Strongin, P. T. Lewis, K. K. Kim, N. N. St. Luce, A. A. Mrse, C. J. Davis and F. R. Fronczek, Chromophore formation in resorcinarene solutions and the visual detection of mono- and oligosaccharides, *J. Am. Chem. Soc.*, 2002, **124**, 5000–5009.

41 I. Maisuls, S. Ostendorp, G. Wilde, A. J. J. Parola, C. A. Strassert and E. Wolcan, Energy Transfer between CNT Surface and –Re(CO) 3 (phen) + * Pendants Grafted to P4VP in Nanohybrid Shish-Kebob-like Structures, *J. Phys. Chem. C*, 2020, **124**, 1238–1248.

42 H. Martens, J. P. Nielsen and S. B. Engelsen, Light scattering and light absorbance separated by extended multiplicative signal correction. Application to near-infrared transmission analysis of powder mixtures, *Anal. Chem.*, 2003, **75**, 394–404.

43 H. Martens and E. Stark, Extended multiplicative signal correction and spectral interference subtraction: New preprocessing methods for near infrared spectroscopy, *J. Pharm. Biomed. Anal.*, 1991, **9**, 625–635.

44 A. Sillen and Y. Engelborghs, The Correct Use of ''Average'' Fluorescence Parameters, *Photochem. Photobiol.*, 1998, **67**, 475–486.

45 P. Shahgaldian, D. Elend and U. Pieles, Para-carboxy modified amphiphilic calixarene, self-assembly and interactions with pharmaceutically-relevant molecules, *Chimia*, 2010, **64**, 45–48.